Krypton-Xenon Separation Properties of SAPO-34 Zeolite Materials and Membranes

Yeon Hye Kwon, Christine Kiang, Emily Benjamin, Phillip Crawford, and Sankar Nair
School of Chemical & Biomolecular Engineering, Georgia Institute of Technology, Atlanta, GA 30332-0100

Ramesh Bhave
Oak Ridge National Laboratory, Materials Science & Technology Division, Oak Ridge, TN 37831

DOI 10.1002/aic.15434
Published online July 27, 2016 in Wiley Online Library (wileyonlinelibrary.com)

Separation of the radioisotope ^{85}Kr from ^{136}Xe is an important target during used nuclear fuel recycling. We report a detailed study on the Kr and Xe adsorption, diffusion, and membrane permeation properties of the silicoaluminophosphate zeolite SAPO-34. Adsorption and diffusion measurements on SAPO-34 crystals indicate their potential for use in Kr-Xe separation membranes, but also highlight competing effects of adsorption and diffusion selectivity. SAPO-34 membranes are synthesized on α−alumina disk and tubular substrates via steam assisted conversion seeding and hydrothermal growth, and are characterized in detail. Membrane transport measurements reveal that SAPO-34 membranes can separate Kr from Xe by molecular sieving, with Kr permeabilities around 50 Barrer and mixture selectivity of 25–30 for Kr at ambient or slight sub-ambient conditions. The membrane transport characteristics are modeled by the Maxwell-Stefan equations, whose predictions are in very good agreement with experiment and confirm the minimal competing effects of adsorption and diffusion. © 2016 American Institute of Chemical Engineers *AIChE J*, 63: 761–769, 2017
Keywords: zeolite membrane, gas separation, krypton, xenon, SAPO-34

Introduction

Nuclear fission is a large and economical means of producing low-carbon energy and reducing dependence on fossil fuels.[1,2] However, environmentally sustainable nuclear energy production requires complex systems for used nuclear fuel (UNF) recycling and waste management, in particular the efficient treatment of radioactive waste products generated during fission of uranium and plutonium.[3] During the initial mechanical treatment (shearing and chopping) and chemical dissolution (e.g., using nitric acid) of UNF, several fission products trapped in the fuel are released as off-gases in a mixture with other by-products of the recycling pathway.[4] The off-gas is composed of various species including ^{129}I (radioisotope), NO, NO_2, CO_2 containing ^{14}C (radioisotope), ^3H_2O (radioactive tritium oxide), ^{85}Kr (radioisotope), ^{136}Xe, and air. Fission products such as ^{129}I, ^3H_2O, and ^{85}Kr with long decay half-lives (ranging from decades to millions of years) must be stored as waste, for which purpose it is critical to separate them with high purity so that the volume of storage waste can be minimized. Adsorption processes using nanoporous materials (e.g., zeolites and carbons) are currently in existence for removal of gases such as ^{129}I and CO_2 containing ^{14}C.[5–7] There are also significant challenges in separation of the noble gases ^{85}Kr and ^{136}Xe. Adsorbents such as metal-organic frameworks (MOFs) have shown potential for concentrating Kr and Xe from their dilute mixture with other off-gas components such as nitrogen or air.[8–11] However, the concentrated noble gases from UNF reprocessing are typically obtained as mixtures of ~10 mol % Kr/90 mol % Xe, and have been stored as waste in this form.[6,12] Efficient separation of ^{85}Kr would greatly reduce (by a factor of 10) its waste storage volume. Xe is also a commercially valuable gas used in lighting, lasers, medical diagnostics, and NMR spectroscopy. A typical 800 ton heavy metal (tHM)/yr UNF reprocessing facility would release about 3.7 tons Xe/year, corresponding to $16–20 mn/year of pure Xe if recovered in pure form with negligible ^{85}Kr contamination. Additionally, EPA regulations[13,14] specify limits on ^{85}Kr emissions as well as dose limits for workers and the public.

Conventionally, separation of Kr and Xe is conducted by cryogenic distillation.[15] Due to the low boiling points (Kr: 120 K, Xe: 165 K), cryogenic distillation has high capital and operating costs and is not considered suitable for use in UNF recycling. Nanoporous adsorbents have the drawback of being Xe-selective and hence require large bed volumes to completely adsorb the majority component. Although the radiation stability of polymeric materials and membranes is generally low, they have been tested for Kr/Xe separation. For example, silicone elastomer membranes were found to have a Kr permeability of 3.3×10^{-13} mol/m·s·Pa (985 Barrer, where 1 Barrer = 3.348×10^{-16} mol/m·s·Pa) and selectivity for Xe of ~2.30 at 293 K,[15] which was considered unfavorable. Conversely, zeolitic molecular sieve membranes offer an

Additional Supporting Information may be found in the online version of this article.

Corrections added on 12 August 2016, after first online publication.

Correspondence concerning this article should be addressed to S. Nair at sankar.nair@chbe.gatech.edu.

opportunity to exploit the size difference of Kr (kinetic diameter 0.36 nm) and Xe (0.396 nm) to obtain preferential permeation of the minority component (Kr) from the mixture, thereby achieving an efficient separation with low energy requirements. Further, zeolitic and other ceramic materials are already used in UNF reprocessing and are known to be resistant to radiation degradation.[16–19] However, there is no information in the literature on Kr/Xe separations using zeolite membranes. Here we report a detailed study on the Kr and Xe adsorption, diffusion, and membrane permeation properties of the silicoaluminophosphate zeolite SAPO-34, which has previously been studied especially for CO_2/CH_4 separations.[20–22] We hypothesized that SAPO-34 membranes can separate Kr and Xe since the pore size of SAPO-34 (0.38 nm) is intermediate between the kinetic diameters of the two gases. However, there are several interesting differences between Kr/Xe separation and CO_2/CH_4 separation with small-pore zeolite (e.g., SAPO-34) membranes. The Kr/Xe case is more challenging since it is expected to be influenced by competing effects of diffusion selectivity (favoring Kr) and adsorption selectivity (favoring Xe),[23–25] whereas in the CO_2/CH_4 case the diffusion and adsorption selectivities both favor CO_2. In this work, we synthesize SAPO-34 materials and membranes and evaluate the above issues through a detailed study of their adsorption, diffusion, and permeation properties using experimental techniques as well as modeling methods based on the Maxwell-Stefan equations of single-component and binary permeation in zeolite membranes.[26] The results from the latter methods are especially valuable for process modeling calculations targeting the design of a membrane system for Kr/Xe separation. An additional feature of our SAPO-34 membrane synthesis is the demonstration of the steam-assisted conversion (SAC) seeding method to fabricate selective zeolite membranes on low-cost macroporous ceramic substrates. The SAC technique was first introduced by Zhou et al.,[27] and involves the transformation of a reactant paste/gel containing SAPO-34 seed crystals into a compact seed layer with the aid of steam. Here we have shown in detail the use of the SAC method to prepare SAPO-34 membranes with high Kr/Xe selectivities.

Experimental Section

Synthesis of SAPO-34 crystals

SAPO-34 crystals were prepared for two purposes: (1) adsorption and diffusion measurements and (2) seeding the α-alumina substrate for membrane synthesis. Larger SAPO-34 crystals were synthesized from a reactant molar composition of 1.0 Al_2O_3:1.0 P_2O_5:0.32 SiO_2:1.0 TEAOH:1.6 CHA (cyclohexylamine):52 H_2O with alumina hydroxide ($Al(OH)_3$) as the Al source. Smaller SAPO-34 crystals were also prepared from a mixture with molar composition of 1.0 Al_2O_3:1.0 P_2O_5:0.32 SiO_2:1.0 TEAOH:1.6 DPA (diropylamine):52 H_2O. In this case, the Al source was alumina isopropoxide (Al(i-Pr)$_3$). In both syntheses, the P source was phosphoric acid (H_3PO_4, 85 wt % in water) and the Si source was LUDOX AS-40 colloidal silica (40 wt % suspension in water). The structure directing agents (SDAs) were tetraethylammonium hydroxide (TEAOH, 35 wt % in water), cyclohexylamine (CHA, 99% pure) and dipropylamine (DPA, 99% pure). All chemicals were purchased from Sigma-Aldrich and used as received. In a typical synthesis method, the Al source, P source and water were stirred for 3 h to obtain a clear solution and then the Si source was added and the mixture stirred for another 3 h. The SDAs were then added and the synthesis gel solution was aged for 4 days at room temperature. Both types of SAPO-34 crystals were hydrothermally synthesized at 493 K for 6–24 h in Teflon-lined autoclave reactors (Parr) and calcined at 823 K in stagnant air for 6 h to remove the SDAs.

Synthesis of SAPO-34 membranes

Disk-type α-alumina supports (25.4 mm diameter and 1 mm thickness, Coorstek) and tube-type α-alumina supports (11 mm OD, 8 mm ID, 30 mm length, Ceramco) were cleaned by sonication in acetone for 10 min and dried in an oven at 100°C for 24 h before use. The substrates were seeded using the smaller-size SAPO-34 crystals via the SAC method reported by Zhou et al.[27] The seed crystals were added to a synthesis mixture that had a molar composition of 1.0 Al_2O_3:2.0 P_2O_5:0.6 SiO_2:4.0 TEAOH:75 H_2O, and the Al source was alumina isopropoxide and LUDOX AS-40 was used as Si source. The seeds/synthesis mixture ratio was 15 mg/g. After evaporating 90% water from the mixture at 353 K and converting the synthesis mixture into a gel-like paste, the disk support was hand-coated with the paste containing the seeds. For the tubular substrate, the inner surface was coated with the paste. The substrates were then dried for 2 h at 323 K and subsequently placed in Parr autoclaves with 5 mL of DI water introduced at the bottom. The SAC process was then carried out at 473 K for 24 h to convert the paste coating into continuous seed layer.

Well-intergrown SAPO-34 membranes were then prepared from the post-SAC substrates by contacting them with a synthesis mixture of molar composition 0.85 Al_2O_3:1.0 P_2O_5:0.3 SiO_2:1.75 TEAOH:155 H_2O. $Al(OH)_3$ (Al source) and DI water were mixed and stirred for 30 min, followed by phosphrous source addition and stirring for 2 h. The Si source (colloidal silica) was added to the mixture and stirred for additional 30 min. Then TEAOH was added and the mixture was aged for 12 h at 328 K. The seeded substrate was placed vertically in a Parr autoclave and hydrothermal growth was carried out at 493 K for 6 h. The outer surfaces of the tubes were tightly wrapped in Teflon tape before immersion in the synthesis mixture, so that the membrane growth can occur only at the inner surfaces. The membranes were calcined at 873 K for 6 h in stagnant air using a slow 0.5 K/min heating and cooling rate to avoid potential cracks caused by rapid temperature changes. For comparison, disk membranes seeded by the conventional rubbing method[28] and tubular membranes seeded by dip coating (from a colloidal solution of small SAPO-34 crystals)[22] were also prepared.

Structural Characterization. X-ray diffraction (XRD) patterns of synthesized crystals and membranes were obtained using a PANalytical X'pert diffractometer operating with a Cu-Kα source in a scanning range of 5–40° 2θ. The surface and cross-section morphologies of crystals and membranes were observed by scanning electron microscopy (SEM) on a JEOL LEO-1530 at a landing energy of 10 kV using an InLens detector. Crystal size distributions were obtained from statistica analysis of multiple SEM images. N_2 adsorption–desorption isotherms were measured with a Tristar II 3020 (Micromeritics).

Adsorption and Diffusion Measurements and Analysis. The single-gas adsorption isotherms and transport diffusivities were measured in a pressure decay cell (PDC) built in-house.[29,30] A known amount of sample was degassed at 293 K 120°C for 12 h in vacuum prior to measurement. Adsorption

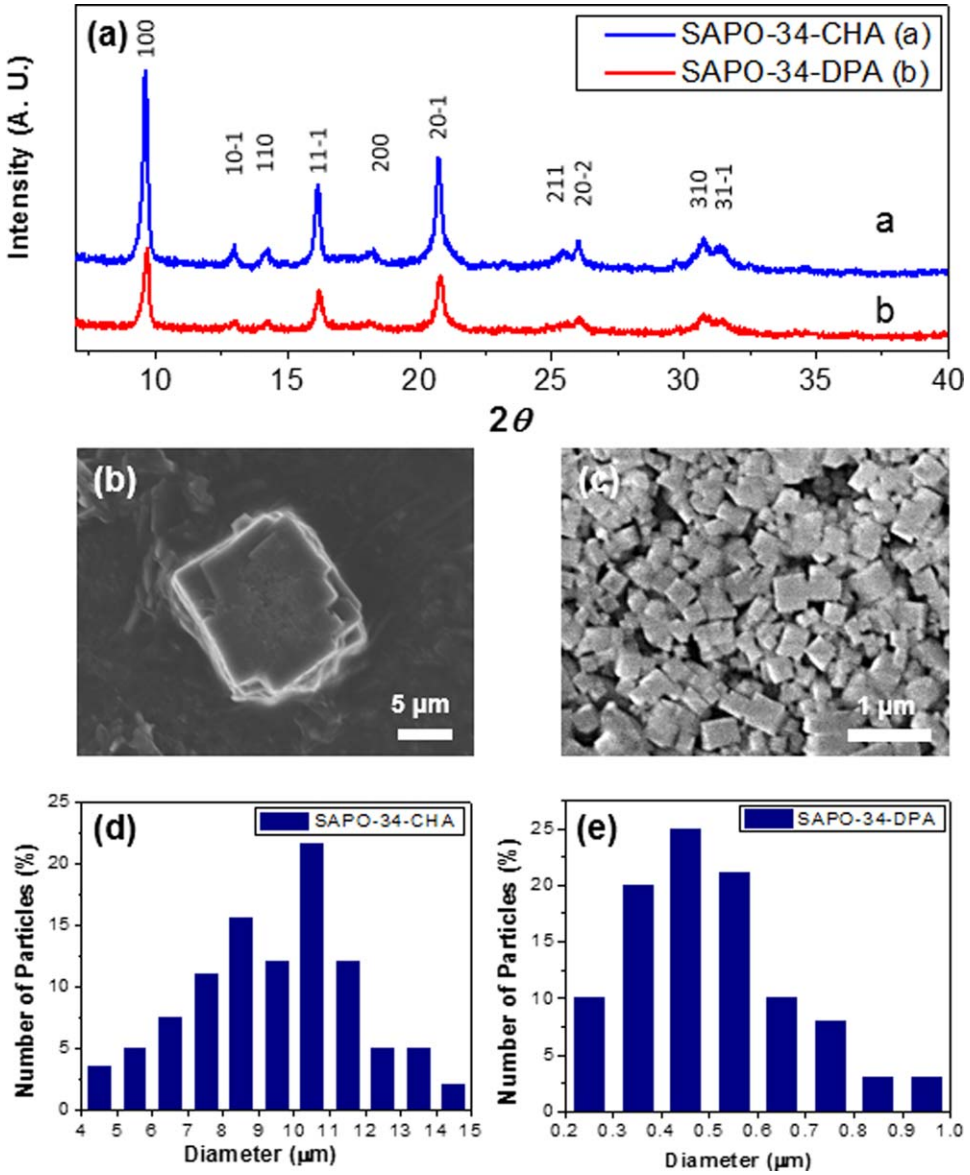

Figure 1. (a) XRD patterns of larger crystals (SAPO-34-CHA) and smaller crystals (SAPO-34-DPA) as a function of 2θ diffraction angle; (b–c) example SEM images of both types of crystals showing the characteristic SAPO-34 cuboidal shape; and (d–e) crystal size distributions of both types of crystals. The "crystal diameter" is defined as discussed in the results and discussion section.

[Color figure can be viewed in the online issue, which is available at wileyonlinelibrary.com.]

isotherms were measured at temperatures from 308 to 343 K and the isotherm data were fitted to the Langmuir model (Supporting Information, Section 1, Eq. S1).[21] Here q is the adsorbate concentration in the sample, q_{sat} the saturation coverage, p the pressure, and b the Langmuir constant which can be expressed in terms of the enthalpy of adsorption (ΔH_{ads}) and the pre-exponential entropic factor $b_o = \exp(\Delta S_{ads}/R)$. These values were obtained by fitting to the b values using isotherms measured at three different temperatures (308, 323, 343 K). Since membrane separation occurs under mixture conditions, we also used the Langmuir-fitted single-component isotherms to predict the binary adsorption behavior *via* ideal adsorbed solution theory (IAST).[31] The IAST equilibrium relationship (Supporting Information, Section 1, Eqs. S2–S4) for solid-fluid equilibrium is analogous to Raoult's law for vapor-liquid equilibrium. We hypothesized essentially ideal mixing in the adsorbed phase, which is an excellent assumption for noble gas mixtures in non-cationic zeolites. The adsorbed amounts of gas as well as total adsorbed amounts were calculated at different conditions of Kr-Xe mixture composition, total pressure, and temperature. A computer code was written to generate these predictions, according to the details of practical application of IAST as described in detail elsewhere.[31,32] The double Langmuir approximation (Supporting Information, Section 1, Eq. S5) was also used for comparison to the IAST predictions. Transport (Fickian) diffusivities were measured from the PDC data by fitting the kinetic gas uptake curves at low loadings of the gas in the zeolite. The model used has been described in detail previously[29,33] (also see Supporting Information, Section 2, Eq. S6 and Figure S1) and accounts for the crystal size distributions as well as the time-dependent pressure boundary condition. The thermodynamically corrected Maxwell-Stefan (M-S) diffusivity, which can be taken as representing the intrinsic rate of diffusive hopping of

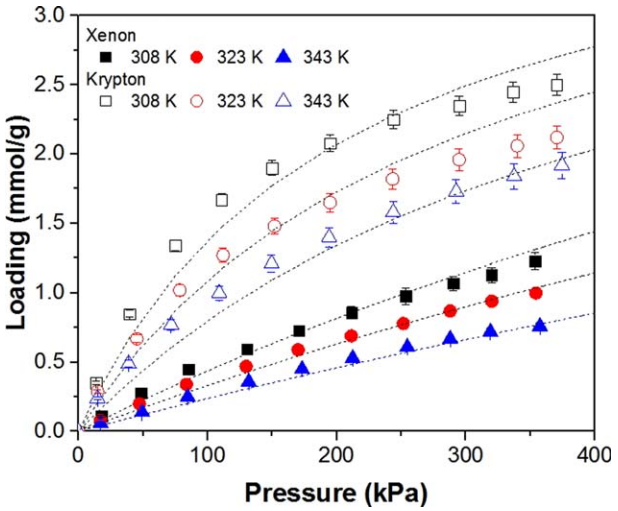

Figure 2. Single-gas Kr and Xe adsorption isotherms on SAPO-34.

Symbols: experimental data, dashed lines: Langmuir fits. [Color figure can be viewed in the online issue, which is available at wileyonlinelibrary.com.]

molecules in the zeolite pores, is then obtained from the Fickian diffusivity (Supporting Information, Section 2, Eqs. S7 and S8).[34–36] The diffusion activation energy (E_a) and pre-exponential part (D^o_{MS}) of the M-S diffusivity are obtained from diffusivity measurements at three different temperatures (308, 323, 343 K) via fitting to the Arrhenius relation.

Permeation Measurements. Single-component permeation measurements were carried out on disk and tube-type SAPO-34 membranes using in-house built permeation units operating in dead-end mode (Supporting Information, Figure S2). Various gases were measured at ambient temperature (295 K), but Kr and Xe permeation measurements were additionally conducted at temperatures ranging from 254 to 343 K. For sub-ambient operation, the membrane module was submerged in a salt water-ice cooling bath at 254 K. Prior to measurement, the membranes were degassed *in situ* under vacuum at 373–473 K for 1–4 h prior to measurement. The feed pressure was maintained at 110 kPa and the permeate side was at vacuum. The fluxes were obtained by the standard method of measuring the rate of the initial linear pressure rise in a collection vessel on the permeate side after isolating the vacuum. The permeance is then obtained as the ratio of the measured flux and the pressure drop between the feed and permeate side. Finally, the ideal selectivity (permselectivity) of Kr over Xe is the ratio of their respective permeances. Binary mixture permeation was measured in a Wicke-Kallenbach mode at a system pressure of 1 atm (Supporting Information, Figure S3). The feed was 10 mol % Kr/90 mol % Xe mixture, generated by two mass flow controllers. The total flow rate of feed was 30 mL/min. A helium sweep (20 mL/min) was used to collect the permeate, whose composition was then analyzed by a gas chromatograph (Shimadzu GC-TCD-2014) equipped with a HP-PLOT 5A column (Agilent) and a TCD. The permeance of each component is obtained as its flux normalized by its transmembrane partial pressure. The Kr/Xe selectivity of the membrane is given as the ratio of permeances of each gas.

Results and Discussion

Figure 1a shows XRD patterns of the larger crystals (labeled SAPO-34-CHA) made with the cyclohexamine (CHA) SDA and the smaller crystals (labeled SAPO-34-DPA) made with dipropylamine (DPA) SDA. Both materials show the characteristic diffraction peaks of the SAPO-34 structure. Image analysis of a number of SEM micrographs (e.g., Figures 1b,c) allows the quantification of crystal size distributions (Figures 1d,e) for each material. The average crystal sizes and standard deviations are 10.7 ± 2.3 μm (SAPO-34-CHA) and 0.5 ± 0.1 μm (SAPO-34-DPA), respectively. The edge dimension of the cuboid crystals is used as the effective crystal diameter, since this achieves the required equivalence of surface area-to-volume ratio with a spherical crystal of the same diameter. The large crystals are used for measuring adsorption and diffusion behavior since they eliminate (or mitigate) the possibility of external and intercrystalline mass transfer resistances, whereas the small crystals are used for seeding the membrane substrates. N_2 physisorption measurements at 77 K on the calcined large crystals showed a micropore volume of 0.22 cm^3/g and BET surface area of 490 m^2/g, both of which are in good agreement with previous literature.[21] The micropore volume is especially important in confirming that the calcination procedure leads to effective removal of the SDA from the pores.

Figure 2 shows the experimental single-component Kr and Xe adsorption isotherms collected at three different temperatures over the pressure range 10–400 kPa. SAPO-34 shows preferential adsorption of Xe over Kr (e.g., by a factor of roughly 3 at 100 kPa). The Langmuir adsorption thermodynamic parameters (obtained from a global fit of the isotherms over all three temperatures) are collected in Table 1. The enthalpy and entropy of adsorption of Xe in SAPO-34 are higher than that of Kr, thus leading to stronger adsorption of Xe. Overall the Langmuir model provides an excellent fit of the adsorption isotherms, and we therefore use it directly in the IAST calculations. Figure 3 shows the IAST predictions of binary adsorption from a 10/90 Kr/Xe feed gas mixture at two temperatures (298 K and a sub-ambient temperature of 254 K) for pressures up to 500 kPa. The selectivity is defined as described in the Supporting Information (Eq. S4). The IAST-predicted binary adsorption selectivity for Xe is significantly higher (e.g., ~4 at 298 K and 100 kPa) than that predicted by a simple weighting of the single-component isotherms (~3). Thus in a binary mixture, Xe is preferentially adsorbed and blocks the adsorption site of Kr in the binary mixture. Furthermore, the Xe adsorption selectivity decreases slightly with increasing pressure. Therefore, to allow the expected Kr diffusion selectivity to counteract the Xe adsorption selectivity, the

Table 1. Langmuir Adsorption Parameters and Maxwell-Stefan Diffusion Parameters for Kr and Xe in SAPO-34 as Obtained from Experimental Adsorption Isotherms and Kinetic Uptake Data

Gas	q_{sat} (mmol/g)	$-\Delta H_{ads}$ (kJ/mol)	b_0 ($\times 10^{-6}$ kPa^{-1})	D^0_{MS} ($\times 10^{-10}$ m^2/s)	E_a (kJ/mol)
Kr	6.1 ± 0.2	16.1 ± 0.3	1.4 ± 0.3	2.5 ± 0.3	13.9 ± 1.0
Xe	4.2 ± 0.1	18.3 ± 0.4	3.8 ± 0.2	2.0 ± 0.1	23.6 ± 0.8

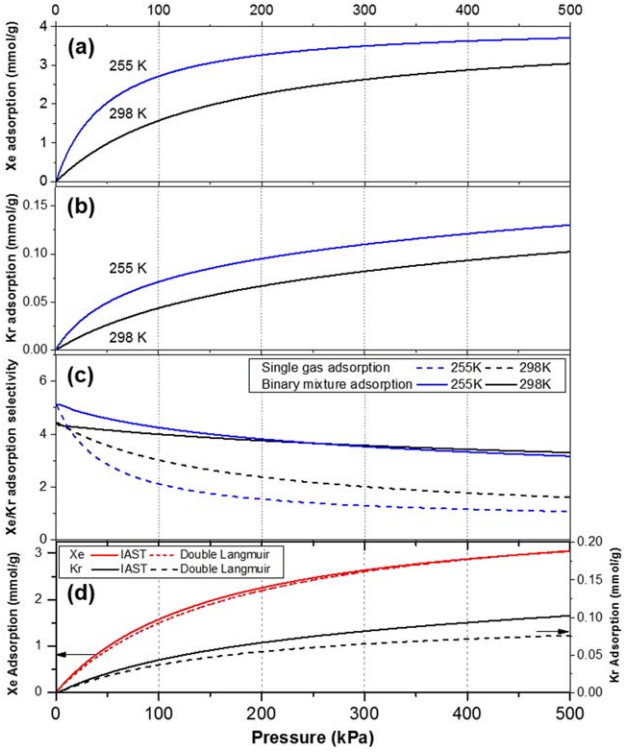

Figure 3. IAST predictions of (a) Xe and (b) Kr adsorption on SAPO-34 from a 10/90 Kr/Xe binary feed mixture; and (c) the corresponding Xe/Kr adsorption selectivity; at two temperatures of 255 and 298 K. (d) Comparison between double Langmuir approximation and IAST predictions at 298 K.

[Color figure can be viewed in the online issue, which is available at wileyonlinelibrary.com.]

membrane is best operated at atmospheric or higher pressure conditions. The IAST predictions were then used for comparison with the double Langmuir model (Supporting Information, Eq. S5). The parameters used in the double Langmuir model are, by definition, the same as those already obtained from the single-component Langmuir isotherms. This comparison is useful because the double Langmuir model (unlike the IAST) is very convenient for use in Maxwell-Stefan modeling of membrane transport owing to its simple mathematical form as well as the ease of deriving analytical expressions for the thermodynamic correction factors. As shown in Figure 3d, the double Langmuir isotherm matches very well with the IAST predictions for Xe over the entire pressure range and for Kr at atmospheric or lower pressures (<100 kPa). Since this study focuses on Kr-Xe separation from a feed at atmospheric pressure conditions, Figure 3d indicates that the double Langmuir model is acceptable for use in Maxwell-Stefan modeling of transport in the SAPO-34 membrane. Table 1 also shows the M-S diffusion parameters obtained from the kinetic uptake data (see Supporting Information). While the D_{MS}^{0} values for Kr and Xe are similar in magnitude, the diffusion activation energy of Kr is much lower than that of Xe. This is consistent with the kinetic diameters of Kr (0.36 nm) and Xe (0.396 nm) in relation to the crystallographic pore size of SAPO-34 (0.38 nm).[21,37]

Various seeding methods including rub-coating,[38] dip-coating,[20–22] and vacuum seeding[39] have been reported for zeolite membrane fabrication. The rub-coating method has been widely used for SAPO-34 membranes. However, Zhou et al. recently reported that SAPO-34 membranes seeded by SAC showed a smooth and continuous morphology with high H_2 permeance of 6.96×10^{-8} mol m^{-2} s^{-1} Pa^{-1} (or 208 GPU, where 1 Gas Permeation Unit = 3.348×10^{-10} mol m^{-2} s^{-1} Pa^{-1}) and a good H_2/CH_4 single-gas selectivity of 15.[27] Based on this initial report, we employed SAC as a seeding method for the fabrication of SAPO-34 membranes discussed in this report. Figure 4 shows SEM images of the α-Al_2O_3 disk substrate (Figures 4a,b) and the SAPO-34 membrane after SAC seeding (Figures 4c,d) and final hydrothermal growth (Figures 4e,f). The SAC method is seen to provide a continuous and dense "seed" covering, and is particularly useful for coating low-cost α-Al_2O_3 supports such as those used here. Such supports typically display large ($\sim$1 μm) particles of alumina sintered together with pores in between (rather than a more uniformly porous surface obtained from packing of smaller alumina particles), which makes it difficult to obtain good seed coverage using conventional dip-coating or rub-coating seed methods. The seed layer does not grow beyond a few hundreds of nm, since there is only a limited supply of reactants available in the initial gel paste coated on the substrate. Finally, continuous membranes were synthesized containing

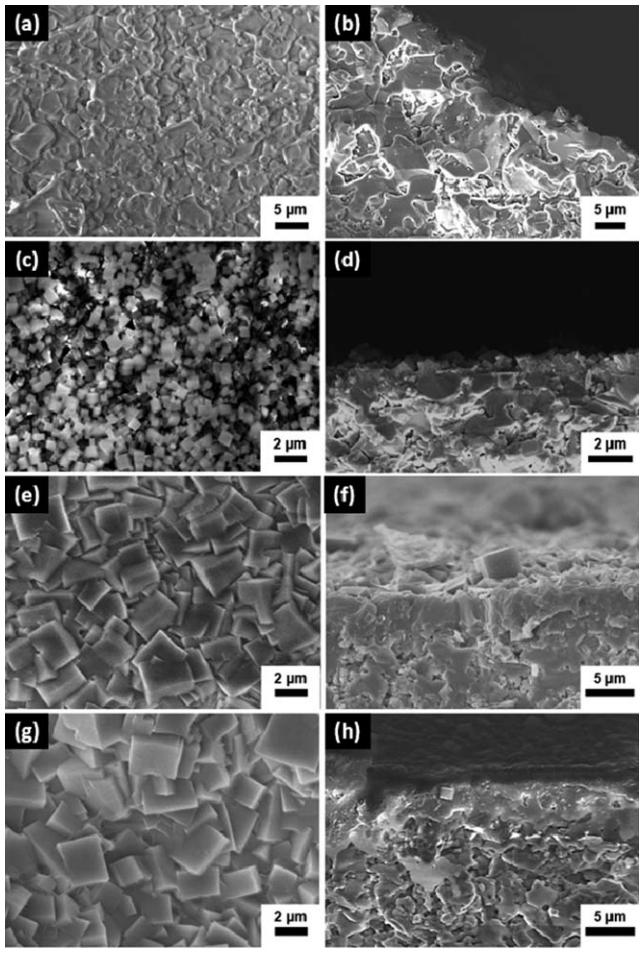

Figure 4. Top view and cross-section SEM images of (a, b) α-alumina disk support, (c, d) SAC seed layer, (e, f) final SAPO-34 membrane, and (g, h) final SAPO-34 membrane synthesized by the same technique on tubular α-alumina support.

Table 2. Effect of Membrane Seeding Method on Single-Gas Kr and Xe Permeances at 295 K

Sample	Permeance Kr (10^{-10} mol/m^2·s·Pa)	Xe	SF_6	Ideal selectivity Kr/Xe
Bare disk support	7130	6220	–	1.1
Bare tube support	6860	5730	–	1.2
SAPO-34 disk (rub coat seeded)	38.8	8.1	3.8	4.8
SAPO-34 disk (SAC seeded)	26.2	1.5	0.1	13.8
SAPO-34 tube (dip coat seeded)	31.5	7.7	4.2	4.1
SAPO-34 tube (SAC seeded)	37.4	2.1	0.1	17.8

interlocked cuboidal crystals of 1–3 μm size. The final membrane thickness was determined as 4.9 ± 0.2 μm based on the average of SEM-measured thicknesses at different cross-sectional locations. The SAC and hydrothermal growth was then successfully transferred to tubular supports, and the resulting membranes are shown in Figures 4g,h. The tubular membrane thickness was determined as 4.1 ± 0.1 μm.

Table 2 compares the single-gas permeances of Kr, Xe, and SF_6 (kinetic diameter 0.55 nm) in the bare alumina supports and the SAPO-34 membranes synthesized after dip-coat seeding and SAC seeding. SF_6 is included as a sensitive probe of membrane quality since it is much larger than the pore size of SAPO-34. As expected, the bare alumina supports have permeances that are orders of magnitude higher than those of the molecular sieving membranes. Compared to the conventional dip-coat seeding method, the membranes synthesized by steam-assisted seeding method shows 4–8 times higher selectivity for Kr over Xe because of the reduction in defects resulting from the high quality seed layer. The significant level of SF_6 permeance reveals the presence of nanoscale defects in the membranes synthesized with conventional dip-coating. The SF_6 permeance drops by more than an order of magnitude when using the SAC method.

Figure 5 shows the single-gas permeances through the SAC-seeded SAPO-34 disk and tube membranes at 295 K as a function of molecular kinetic diameter. The trends in permeance are the same in disk and tubular membranes, showing a successful transfer of the membrane synthesis from disk to tubular supports. Even though H_2 has the smallest kinetic diameter, CO_2 shows the highest permeance due to its strong adsorption in SAPO-34.[21] We can also compare these permeances to other reported literature data. For example, the permeability of CO_2 through the disk membrane is 4.0×10^{-13} mol m m^{-2} s^{-1} Pa^{-1} (1200 Barrer), which is comparable to the range of reported literature values of $2.0–9.2 \times 10^{-13}$ mol m m^{-2} s^{-1} Pa^{-1} (600–2700 Barrer).[22,40,41] Similarly, the H_2 permeability of the disk membrane was 1.8×10^{-13} mol m m^{-2} s^{-1} Pa^{-1} (520 Barrer) which is in the range of reported values (300–600 Barrer).[40] The CO_2 permeances as well as ideal selectivities of different gas pairs at 295 K are listed in Table 3. The CO_2 permeances and ideal selectivities of H_2/CH_4, CO_2/CH_4, and Kr/Xe are all high, confirming the high quality of the membranes. Furthermore, these data compare well to the data available in the reported literature.

Figure 6 shows the temperature dependence of single-gas permeation of Kr and Xe through the disk (Figure 6a) and tubular (Figure 6b) membrane. The single gas permeance of Kr decreases with increasing temperature, whereas the Xe permeance increases. The temperature dependence of permeance results in the highest ideal selectivity of 23 at the sub-ambient temperature and the lowest ideal selectivity of 12 at 343 K. This behavior is due mainly to Kr transport being controlled by adsorption (since diffusion of Kr is already fast) versus Xe transport controlled by activated diffusion (since it has a high activation energy). We then modeled the temperature dependence of the Kr/Xe permeances and ideal selectivities using the Maxwell-Stefan equation for single-component transport across the membrane (Supporting Information, Section 3, Eq. S9). The adsorption and diffusion parameters in Table 1 were used for these predictions, whose results are shown as solid lines in Figure 6. Overall, the model predictions are in very good agreement with the experimental data, and they correctly predict the magnitude and the temperature dependence of the permeances of both Kr and Xe. It is also important to note that the M-S permeation equation used here corresponds to the regime in which the M-S diffusivity is essentially independent of adsorption loading, i.e., the hopping rate of a molecule is not significantly affected by the presence of other molecules. The correctness of this assumption is corroborated by several factors. First, we have also predicted the temperature dependence using the M-S equation for the opposing case in which the M-S diffusivity is taken as a linearly decreasing function of the loading and approaches zero as the saturation capacity is reached.[42] However, this equation does not correctly predict the temperature dependence or the magnitude of the permeances. Second, the adsorption isotherms (Figure 2) show that a membrane operating at a feed pressure of 100 kPa and vacuum on the permeate side is quite far from saturation loading of either Kr or Xe. Finally, other researchers have recently proposed the same explanation for gas permeation through other small-pore zeolite or MOF materials, based on experimental and molecular simulation data.[11]

Some quantitative deviation in the selectivity value is seen at sub-ambient conditions (254 K). This may be due to the fact that the selectivity (in this case) is a ratio of a large and a small permeance value, which becomes highly sensitive to the Xe

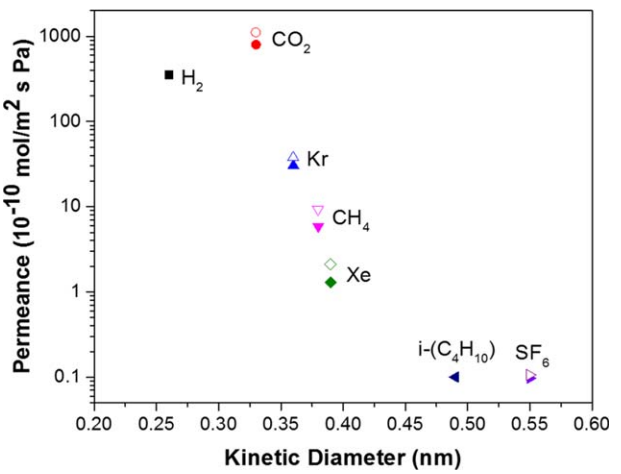

Figure 5. Single-gas permeances of different gases at 295 K in SAPO-34 disk and tubular membranes at a feed pressure of 100 kPa.

Closed symbols: disk membrane, open symbols: tubular membrane. [Color figure can be viewed in the online issue, which is available at wileyonlinelibrary.com.]

Table 3. Comparison of Ideal Selectivities of Different Gases at Ambient Temperature and Feed Pressure of 100 kPa

	CO_2 permeance (10^{-7} mol.m^{-2}.s^{-1}.Pa^{-1})	Single-gas permselectivity			
		CO_2/CH_4	H_2/CH_4	H_2/CO_2	H_2/i-C_4H_{10}
This work (disk/tube)	0.8/1.1	116/121	60.6/NR	0.4/NR	2650/NR
Ref. 22	1.3	106	NR	NR	NR
Ref. 39	0.4	NR	NR	0.5	NR
Ref. 40	2.3	150	NR	NR	NR

NR, not reported.

permeability at sub-ambient conditions wherein the Xe permeability is very small. The Xe permeability can be strongly influenced by the presence of even a small number of defects. One way to quantify the extent of defects is to treat the measured permeance of SF_6—a large molecule with kinetic diameter 0.55 nm—as arising entirely from Knudsen diffusion through non-zeolitic pores (defects). The SF_6 permeance is 0.9 $\times$ 10^{-11} mol m^{-2} s^{-1} Pa^{-1} at 254 K. The corresponding Kr and Xe defect permeances are estimated by multiplying with the Knudsen factor (the square root of the ratio of inverse molecular masses, which is equal to 1.31 for Kr and 1.04 for Xe). When the observed permeances of Kr and Xe are corrected by subtracting the estimated defect permeance, the ideal Kr/Xe selectivity is calculated to be marginally higher (26). The time-lag method[43] can also be used to estimate the defect permeance of Xe in the SAPO-34 disk membrane. By this method, the Xe defect permeance was estimated as 4.1 $\times$ 10^{-11} mol m^{-2} s^{-1} Pa^{-1} (see Supporting Information, Section 4, Eq. S10 and Figure S4). The ideal selectivity of a defect-free SAPO-34 membrane at 254 K is extrapolated to be 30, which is closer to the M-S prediction of 39. It is also possible that polycrystalline zeolite films may exhibit some differences in diffusion and adsorption characteristics compared to powder crystals (e.g., due to the existence of tensile or compressive stresses in the film), and these differences may also depend on the membrane type (disk versus tube). However, our main objective in this work was to evaluate whether the MS model—parameterized from adsorption and diffusion measurements on crystals—can quantitatively predict the trends in membrane permeation properties. The results of Figure 6 show that such a hypothesis is overall justified.

Finally, we investigated the separation of a binary Kr/Xe mixture (molar ratio = 10/90) with tubular SAPO-34 membranes. Figure 7 shows the temperature dependence of Kr/Xe binary mixture permeation. Similar to the single gas permeation behavior, the binary Kr permeance decreases slightly with increasing temperature whereas the Xe permeance is small and increases with temperature. A Kr/Xe selectivity of 30 could be obtained at the lowest measured temperature (255 K) and 12 at the highest measured temperature (343 K).

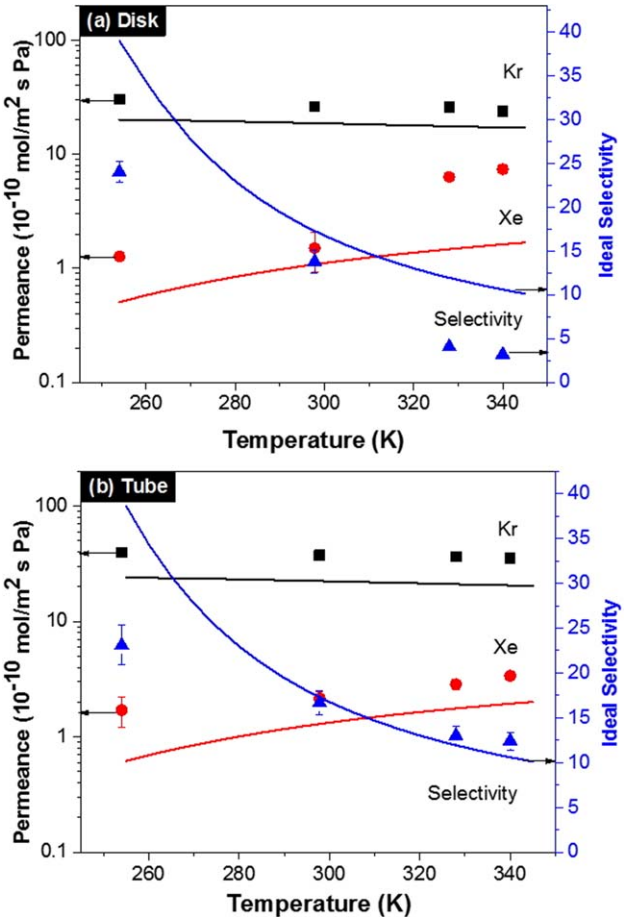

Figure 6. Temperature dependence of Kr and Xe single-gas permeances and ideal Kr/Xe selectivity for (a) disk and (b) tubular SAPO-34 membranes.

Symbols are experimental data and lines are results from the Maxwell-Stefan model predictions. [Color figure can be viewed in the online issue, which is available at wileyonlinelibrary.com.]

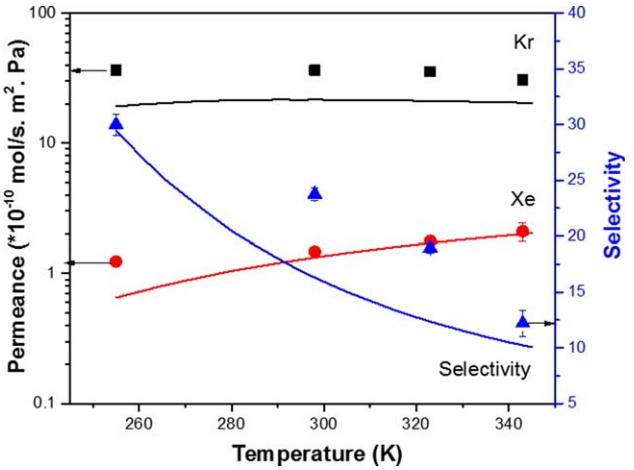

Figure 7. Temperature dependence of Kr and Xe mixture permeances and Kr/Xe mixture selectivity for tubular SAPO-34 membranes. The feed mixture is at 1 atm with 10 vol % Kr/90 vol % Xe.

Symbols are experimental data and lines are results from the Maxwell-Stefan model predictions. [Color figure can be viewed in the online issue, which is available at wileyonlinelibrary.com.]

Compared to single component permeance measurements, the binary mixture separation showed improved performance at all temperatures. This result is clearly promising for the application of SAPO-34 membranes in Kr/Xe separation, but is contrary to our initial speculation that Kr permeation may be slowed down by Xe in the binary mixture thereby decreasing the membrane selectivity. To investigate this finding further, the permeation characteristics of the binary Kr/Xe mixture was modeled using the Maxwell-Stefan equations for two components (Supporting Information, Section 5, Eqs. S11–S13). As discussed earlier, the double Langmuir isotherm was used to approximate the binary mixture adsorption behavior. The predicted membrane characteristics are in good agreement with the experimental results. As in the case of single-gas permeation, the slight difference in selectivity between the M-S model and experimental data was due to the uncertainty in experimental determination of the Xe permeability. The operation of the membrane at slight sub-ambient conditions appears to be quite favorable since the permeance of Kr remains high and the selectivity dramatically increases with decrease in temperature. Furthermore, cooling the membrane to 20–30 K below ambient represents only a small energy cost, especially in comparison to cryogenic distillation.

Conclusions

SAPO-34 membranes that are selective for Kr/Xe separations were prepared on macroporous α-Al_2O_3 substrates via a steam-assisted seeding method followed by hydrothermal growth of polycrystalline membranes. The observed permeance and selectivity behavior of the SAPO-34 membranes were explained in terms of the measured adsorption and diffusion characteristics of each gas in the micropores of SAPO-34. The Maxwell-Stefan model of permeation in zeolite membranes is found to provide predictions that are in good agreement with the experimental results. Although the adsorption selectivity for Xe somewhat reduces the overall membrane selectivity for Kr, this effect is not significantly different in single-component versus binary (mixture) permeation. As a result, the SAPO-34 membranes show high mixture separation performance for Kr over Xe (Kr selectivity 25–30 and Kr permeability ~50 Barrer) at ambient or slight sub-ambient conditions. These findings are expected to be beneficial in the design and development of a membrane system for efficient separation of Kr/Xe mixtures into pure gas streams.

Acknowledgments

This work was supported by the Department of Energy Office of Nuclear Energy (grant number DE-NE 0008298). We are grateful to Dr. R. Jubin, Dr. G. Del Cul, and Dr. E. Collins (all ORNL) for useful discussions, K. Eum and Dr. S. Yang (Georgia Tech) for their assistance in setting up permeation measurements, and V. Pisharodi and J. Hwang (Georgia Tech) for their assistance in adsorption measurements.

Literature Cited

1. Strategy for the management and disposal of used nuclear fuel and high-level radioactive waste. *U.S. Department of Energy*. Washington, DC, 2013.
2. Marques JG. Evolution of nuclear fission reactors: third generation and beyond. *Energ Convs Manage*. 2010;51:1774–1780.
3. Global nuclear energy partnership conceptual design studies: summary (non-proprietary). *GE Hitachi Nuclear Energy*, 2008.
4. Hoffert MI, Caldeira K, Benford G, Criswell DR, Green C, Herzog H, Jain AK, Kheshgi HS, Lackner KS, Lewis JS, Lightfoot HD, Manheimer W, Mankins JC, Mauel ME, Perkins LJ, Schlesinger ME, Volk T, Wigley TML. Advanced technology paths to global climate stability: energy for a greenhouse planet. *Science* 2002;298:981–987.
5. Gombert D, Roach J. Global nuclear energy partnership: integrated waste management strategy; DOE Report GNEP-WAST-WAST-AI-RT-2007-000324, 2007.
6. Haefner D, Law J, Tranter T. System design description and requirements for modeling the off-gas systems for fuel recycling facilities; Idaho National Laboratory: INL-2010. 2010.
7. Jubin RT, DelCul GD, Patton BD, Owens RS, Ramey DW, Spencer BB. Advanced fuel cycle initiative coupled end-to-end research, development, and demonstration project: integrated off-gas treatment system design and initial performance-9226. In: *Waste Management Conference 2009*. Phoenix, AZ, 2009.
8. Banerjee D, Cairns AJ, Liu J, Motkuri RK, Nune SK, Fernandez CA, Krishna R, Strachan DM, Thallapally PK. Potential of metal-organic frameworks for separation of xenon and krypton. *Accounts Chem Res*. 2015;48:211–219.
9. Wang H, Yao K, Zhang Z, Jagiello J, Gong Q, Han Y, Li J. The first example of commensurate adsorption of atomic gas in a MOF and effective separation of xenon from other noble gases. *Chem Sci*. 2014;5:620–624.
10. Lawler KV, Hulvey Z, Forster PM. Nanoporous metal formates for krypton/xenon separation. *Chem Commun*. 2013;49:10959–10961.
11. Fernandez CA, Liu J, Thallapally PK, Strachan DM. Switching kr/xe selectivity with temperature in a metal-organic framework. *J Am Chem Soc*. 2012;134:9046–9049.
12. Moore EB. Control technology for radioactive emissions to the atmosphere at US Department of Energy facilities; Pacific Northwest Laboratory: PNL-4621-Final, 1984.
13. Environmental radiation protection standards for nuclear power operations, 40CFR190.10. *US Environmental Protection Agency*. Washington, DC, 2010.
14. Standards for protection against radiation, 10CFR20. *US Nuclear Regulatory Commission*. Washington, DC, 2012.
15. Stern SA, Leone SM. Separation of krypton and xenon by selective permeation. *AIChE J*. 1980;26:881–890.
16. Ambashta RD, Sillanpaa ME. Membrane purification in radioactive waste management: a short review. *J Environ Radioactiv*. 2012;105:76–84.
17. Watanabe Y, Ikoma T, Yamada H, Suetsugu Y, Komatsu Y, Stevens GW, Moriyoshi Y, Tanaka J. Novel long-term immobilization method for radioactive iodine-129 using a zeolite/apatite composite sintered body. *ACS Appl Mater Interfaces* 2009;1:1579–1584.
18. Dyer A, Keir D. Nuclear waste treatment by zeolites. *Zeolites* 1984;4:215–217.
19. Zakrzewska-Trznadel G, Harasimowicz M, Chmielewski AG. Membrane processes in nuclear technology-application for liquid radioactive waste treatment. *Sep Purif Technol*. 2001;22–23:617–625.
20. Li S, Carreon MA, Zhang Y, Funke HH, Noble RD, Falconer JL. Scale-up of SAPO-34 membranes for CO_2/CH_4 separation. *J Membrane Sci*. 2010;352:7–13.
21. Li S, Falconer JL, Noble RD. SAPO-34 membranes for CO_2/CH_4 separation. *J Membrane Sci*. 2004;241:121–135.
22. Zhou R, Ping EW, Funke HH, Falconer JL, Noble RD. Improving SAPO-34 membrane synthesis. *J Membrane Sci*. 2013;444:384–393.
23. Ianovski D, Munakata K, Kanjo S, Yokoyama Y, Koga A, Yamatsuki S, Tanaka K, Fukumatsu T, Nishikawa M, Igarashi Y. Adsorption of noble gases on H-mordenite. *J Nucl Sci Technol*. 2002;39:1213–1218.
24. Bazan RE, Bastos-Neto M, Moeller A, Dreisbach F, Staudt R. Adsorption equilibria of O_2, Ar, Kr and Xe on activated carbon and zeolites: single component and mixture data. *Adsorption*. 2011;17:371–383.
25. Gurdal Y, Keskin S. Atomically detailed modeling of metal organic frameworks for adsorption, diffusion, and separation of noble gas mixtures. *Ind Eng Chem Res*. 2012;51:7373–7382.
26. Krishna R, van Baten JM. Investigating the influence of diffusional coupling on mixture permeation across porous membranes. *J Membrane Sci*. 2013;430:113–128.
27. Zhou L, Yang J, Li G, Wang J, Zhang Y, Lu J, Yin D. Highly H2 permeable SAPO-34 membranes by steam-assisted conversion seeding. *Int J Hydrogen Energ*. 2014;39:14949–14954.
28. Kassaee MH, Sholl DS, Nair S. Preparation and gas adsorption characteristics of zeolite MFI crystals with organic-functionalized interiors. *J Phys Chem C*. 2011;115:19640–19646.

29. Eum K, Jayachandrababu KC, Rashidi F, Zhang K, Leisen J, Graham S, Lively RP, Chance RR, Sholl DS, Jones CW, Nair S. Highly tunable molecular sieving and adsorption properties of mixed-linker zeolitic imidazolate frameworks. *J Am Chem Soc*. 2015;137:4191–4197.
30. Zimmerman CM, Singh A, Koros WJ. Diffusion in gas separation membrane materials: a comparison and analysis of experimental characterization techniques. *J Polym Sci B Polym Phys*. 1998;36: 1747–1755.
31. Murthi M, Snurr RQ. Effects of molecular siting and adsorbent heterogeneity on the ideality of adsorption equilibria. *Langmuir* 2004; 20:2489–2497.
32. Nugent P, Belmabkhout Y, Burd SD, Cairns AJ, Luebke R, Forrest K, Pham T, Ma S, Space B, Wojtas L, Eddaoudi M, Zaworotko MJ. Porous materials with optimal adsorption thermodynamics and kinetics for CO_2 separation. *Nature* 2013;495:80–84.
33. Zhang C, Lively RP, Zhang K, Johnson JR, Karvan O, Koros WJ. Unexpected molecular sieving properties of zeolitic imidazolate Framework-8. *J Phys Chem Lett*. 2012;3:2130–2134.
34. Krishna R, Paschek D. Separation of hydrocarbon mixtures using zeolite membranes: a modelling approach combining molecular simulations with the maxwell–stefan theory. *Sep. Purif Technol*. 2000; 21:111–136.
35. Kapteijn F, Moulijn JA, Krishna R. The generalized Maxwell-stefan model for diffusion in zeolites: sorbate molecules with different saturation loadings. *Chem Eng Sci*. 2000;55:2923–2930.
36. Krishna R, Broeke LJP. The Maxwell-stefan description of mass transport across zeolite membranes. *Chem Eng J Bioch Eng*. 1995; 57:155–162.
37. Li S, Martinek JG, Falconer JL, Noble RD. High-pressure CO_2/CH_4 separation using SAPO-34 membranes. *Ind Eng Chem Res*. 2005;44: 3220–3228.
38. Peng Y, Zhan Z, Shan L, Li X, Wang Z, Yan Y. Preparation of zeolite MFI membranes on defective macroporous alumina supports by a novel wetting–rubbing seeding method: role of wetting agent. *J Membrane Sci*. 2013;444:60–69.
39. Huang A, Lin YS, Yang W. Synthesis and properties of a-type zeolite membranes by secondary growth method with vacuum seeding. *J Membrane Sci*. 2004;245:41–51.
40. Hong M, Li S, Falconer JL, Noble RD. Hydrogen purification using a SAPO-34 membrane. *J Membrane Sci*. 2008;307:277–283.
41. Zhang Y, Avila AM, Tokay B, Funke HH, Falconer JL, Noble RD. Blocking defects in SAPO-34 membranes with cyclodextrin. *J Membrane Sci*. 2010;358:7–12.
42. Krishna R, Baur R. Modelling issues in zeolite based separation processes. *Sep Purif Technol*. 2003;33:213–254.
43. Burggraaf AJ, Vroon ZAEP, Keizer K, Verweij H. Permeation of single gases in thin zeolite MFI membranes. *J Membrane Sci*. 1998; 144:77–86.

Manuscript received Apr. 23, 2016, and revision received June 24, 2016.